PHYSICAL REVIEW MATERIALS **8**, 044604 (2024)

Tiny Fermi surface with an extremely light mass of ternary chalcopyrite CdSnAs$_2$ revealed by angle-resolved photoemission spectroscopy

Daiki Ootsuki,[1,*] Hiroshi Takatsu,[2] Kohei Funada,[2] Tatsuhiro Ishida,[1] Masashi Arita,[3] Shinichiro Ideta,[4,†]
Kiyohisa Tanaka,[4] Hiroshi Kageyama,[2] and Teppei Yoshida[1]
[1]*Graduate School of Human and Environmental Studies, Kyoto University, Sakyo-ku, Kyoto 606-8501, Japan*
[2]*Department of Energy and Hydrocarbon Chemistry, Graduate School of Engineering, Kyoto University, Nishikyo-ku, Kyoto 615-8510, Japan*
[3]*Research Institute for Synchrotron Radiation Science, Hiroshima University, Higashi-hiroshima 739-0046, Japan*
[4]*UVSOR-III Synchrotron, Institute for Molecular Science, Okazaki 444-8585, Japan*

(Received 8 September 2023; revised 7 February 2024; accepted 1 April 2024; published 25 April 2024)

We report the electronic structure of the ternary chalcopyrite CdSnAs$_2$ using angle-resolved photoemission spectroscopy (ARPES) combined with the band-structure calculation. The tiny Fermi surface (FS) with the Fermi wave number $k_F = 0.012$ Å^{-1} was observed, and the carrier density $n = 1.2 \times 10^{17}$ cm^{-3} was estimated. The deduced carrier density n indicates the electron density parameter $r_s = 240$, which corresponds to the extremely low density limit of the three-dimensional (3D) electron gas. On the other hand, the calculated band structure of CdSnAs$_2$ well reproduced the band gap and the effective mass reported by the Hall measurement, the Shubnikov–de Haas (SdH) oscillation, and the optical measurement, quantitatively. Therefore, the ARPES results indicate that the carrier density n decreases and there is a large deviation between the band calculation and the ARPES band structure. These results reveal that the extremely low electron density can be realized near the surface due to the bulk band-bending effect. Moreover, we found the high Fermi velocity of $v_F = 2.55 \times 10^6$ m/s and the extremely light mass of $m^*/m_0 \sim 0.005$ comparable to the Dirac materials. This suggests that the effective mass m^*/m_0 is reduced due to the effect of the long-range Coulomb interaction in the extremely low-density limit. Our findings provide a venue to investigate the physics of the electron correlation in the extremely low-density electron gas as well as the Wigner crystallization or Anderson localization.

DOI: 10.1103/PhysRevMaterials.8.044604

I. INTRODUCTION

Electron-electron correlation is one of the most fundamental concepts in condensed-matter physics. The simplest correlated electron system is homogeneous three-dimensional (3D) electron gas, which shows very rich and challenging physical phenomena despite its simplicity. The electron gas system is characterized by the electron-density parameter r_s, and the effective mass m^*/m_0 depending on r_s is modified by the electron correlation. The electron correlation in the high-density region ($r_s < 1$) is well established by the random phase approximation (RPA). In contrast, a unified view has not been obtained in the intermediate density region ($2 < r_s < 6$) corresponding to typical metals. The RPA approach reveals the increase of the effective mass monotonically ($m^*/m_0 > 1$), and Hedin's *GW* approximation shows that the effective mass approaches the bare electron mass ($m^*/m_0 \sim 1$) with increasing r_s [1]. For the effective-potential expansion (EPX) method, the screening effect of the Coulomb interaction vanishes and the long-range part $\propto 1/r$ of the Coulomb potential is restored, that is, the exchange term and the correlation term act to compensate each other. The resultant competition between the exchange term and the correlation term induces the effective mass $m^*/m_0 < 1$ [2–4]. In the low-density region, the prediction of the electron crystal by Wigner has led to attractive quantum phases such as paired electron crystal and ferromagnetic liquid at low temperature [5–8]. However, it is not clear whether the effective mass diverges, approaches $m^*/m_0 \sim 1$, or decreases in the extremely low-density limit where the Wigner crystal can be realized ($r_s \sim 100$) at low temperature following the discussion of the intermediate density region. To solve this issue, it is necessary to observe the band dispersion and its effective mass in the low-density state by ARPES measurement. In this context, we focus on the electronic state near the surface affected by band bending in the semiconducting materials where the electron density can be controlled.

In this paper, we show the electronic structure of the ternary chalcopyrite semiconductor CdSnAs$_2$ by means of ARPES. An extremely small electron pocket with $k_F = 0.012$ Å^{-1} was observed at the Brillouin zone (BZ) center. We estimated the carrier density $n = 1.2 \times 10^{17}$ cm^{-3}, corresponding to the low-density limit $r_s = 240$. The Fermi velocity of 2.55×10^6 m/s and the effective mass $m^*/m_0 \sim 0.005$ were estimated from the electron band dispersion, which is strongly modified from those of bulk transport. These values are remarkably comparable to the graphene with the Dirac dispersion. Considering the comparison with the bulk results, the low electron density state is realized near the

---

[*] ootsuki.daiki.4z@kyoto-u.ac.jp

[†] Present address: Research Institute for Synchrotron Radiation Science, Hiroshima University, Higashi-hiroshima 739-0046, Japan.

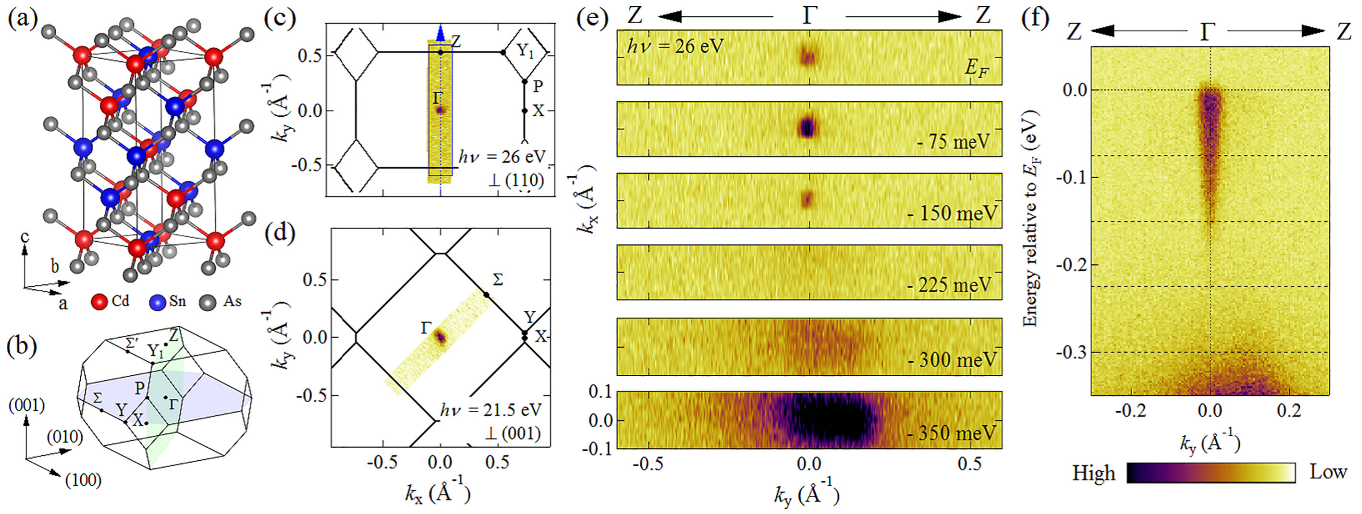

FIG. 1. (a) Crystal structure and (b) Brillouin zone (BZ) of $CdSnAs_2$. The crystal structure of $CdSnAs_2$ is visualized using the software package VESTA [20]. (c), (d) FSs of the $\Gamma XZPY_1$ plane and the $\Gamma XY\Sigma$ plane. The ARPES measurements were performed for the $CdSnAs_2$ (110) plane at $h\nu = 26$ eV and the (001) plane at $h\nu = 21.5$ eV, respectively. (e) ARPES constant energy contours of the blue box area in Fig. 1(c) extracted at different binding energies from E_F to 350 meV. (f) Band dispersion along the Γ-Z direction, which corresponds to the blue arrow in Fig. 1(c). The data were collected at $T = 20$ K.

surface due to the band-bending effect derived from the space-charge accumulation. Our data revealed that the effective mass decreases in the extremely low-density limit at the surface. This provides the experimental evidence for the behavior of the effective mass in the low-density region, which was previously unclear, and it opens up a venue for the electron correlation study in the electron gas system.

A considerable number of studies have been conducted on the semiconducting properties of chalcopyrite compounds. $CdSnAs_2$ is a chalcopyrite II-IV-V_2 type compound with a space group of $I\bar{4}2d$. The crystal structure of $CdSnAs_2$ resembles the zinc-blende structure and consists of two tetrahedra of $CdAs_4$ and $SnAs_4$ as shown in Fig. 1(a). $CdSnAs_2$ shows the n-type semiconducting behavior with a narrow gap of 0.22–0.28 eV [9–13]. The effective mass m^*/m_0 of $CdSnAs_2$ was estimated to be 0.04–0.06 from the bulk transport measurements such as the Hall coefficient and the SdH oscillation [10,11,14–16]. The effective mass is light, and a high carrier mobility of $\sim$12 000 $cm^2/V\,s$ is realized [9]. A recent theoretical study predicted that a 7% decrease of the lattice constant induces the 3D topological state of $CdSnAs_2$ [17]. Moreover, there has also been growing interest in the electric performance and the thermoelectric properties of $CdSnAs_2$ because of the high carrier mobility [13,18,19].

II. EXPERIMENTAL SETUPS

Single crystals of chalcopyrite $CdSnAs_2$ were grown by using the Bridgman method. The SdH oscillation measurement using the same batch of the ARPES measurement exhibits the carrier concentration $n = 3.2 \times 10^{18}$ cm^{-3} with $k_F = 0.036$ Å^{-1} ($r_s = 80$) [21]. The ARPES measurements were performed at BL-9A of HiSOR and BL-7U of UVSOR using a Scienta R4000 analyzer and a MBS Scientific A1 analyzer, respectively. The energy resolution was 15 meV (17 meV) for circular polarized light (linear polarized light) $h\nu = 26$ eV (21.5 eV) and the angular resolution was 0.3° (0.2°) for HiSOR BL-9A (UVSOR BL-7U). The base pressure of the chamber was 2.0×10^{-9} Pa. To obtain a clean surface for the ARPES measurement, the samples were cleaved *in situ* at 20 K along the (110) and (001) planes for ARPES measurements. The binding energy was calibrated by using the Fermi edge of the gold reference. The electronic structure was calculated by using the WIEN2K package [25] based on the full-potential linearized augmented plane-wave (FLAPW) method. The calculated results were obtained in the generalized gradient approximation (GGA) for electron correlations, where we used the exchange-correlation potential [26]. To obtain the insulating ground state, we used the Tran-Blaha modified Becke-Johnson (mBJ) exchange potential [27,28]. We used the crystal structure at room temperature as reported in Ref. [29] and set the muffin-tin radii R_{MT} of 2.5 (Cd), 2.49 (Sn), and 2.39 (As) Bohr and the plane-wave cutoff of $K_{max} = 7.0/R_{MT}$. In the self-consistent calculations, we used 125 k-points in the irreducible part of the BZ. The spin-orbit interaction (SO) was included for all the calculations.

III. RESULTS AND DISCUSSION

Figures 1(c) and 1(d) show the FSs obtained from the different cleavages of $CdSnAs_2$ (110) and (001) surfaces. The tiny FSs were observed at the Brillouin zone (BZ) center even in the different cleavage. We confirmed that the photon energies of $h\nu = 26$ eV for the (110) plane and 21.5 eV for the (001) plane correspond to the BZ center from the photon energy dependence of the normal emission ARPES along the Γ-Z and Γ-Σ lines [21]. Here, the observed FSs strongly depend on the incident photon energy, indicating that it is not the 2D surface state but the 3D electronic state. The evolution of constant energy contour as a function of binding energy (E_B) is plotted in Fig. 1(e). As we moved E_B from E_F to 225 meV, the circular-shaped constant energy contour shrinks gradually (electronlike behavior) and disappears.

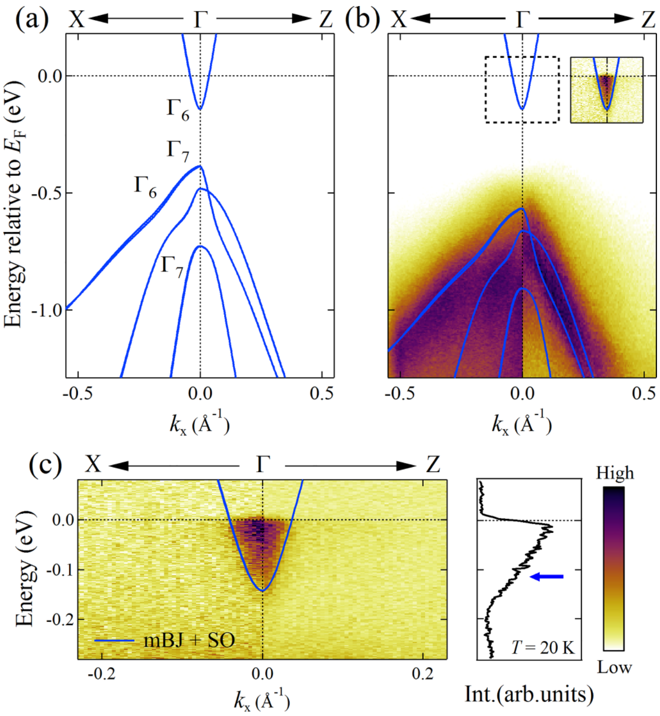

FIG. 2. (a) Band-structure calculation with SO+mBJ of $CdSnAs_2$ along the Γ-X and Γ-Z directions. (b) Band dispersions along the Γ-X and Γ-Z directions compared with the band-structure calculations. The valence bands are shifted down by 180 meV. (c) ARPES spectrum near E_F compared with the band-structure calculations and energy distribution curve (EDC) at the Γ point ($k = 0 \pm 0.025$ Å^{-1}). The arrow indicates the shoulder structure around −110 meV. The ARPES data were obtained from the (110) plane at $h\nu = 26$ eV and the (001) plane at $h\nu = 21.5$ eV, respectively.

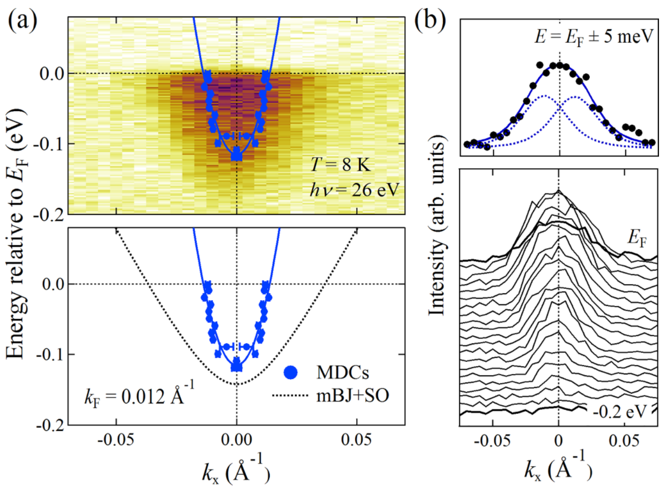

FIG. 3. (a) Near-E_F band dispersion along Γ-Z direction taken at $T = 8$ K and $h\nu = 26$ eV. The dots and the solid line indicate the peak position of the momentum distribution curve (MDC) deduced from the Voigt fitting and its fitted parabolic band dispersion. The fitted result is compared with the band calculation including mBJ + SO. The error bars represent the uncertainty of the peak position. (b) The MDCs of ARPES spectrum of (a). The top panel is the fitted result of MDC at $E = E_F \pm 5$ meV. The bottom panel is the energy dependence of MDC.

Further, moving from $E_B = 300$ to 350 meV, the constant energy contour enlarges (holelike behavior). Figure 1(f) shows the band dispersion along the ΓZ direction. Here, we note that the band dispersion consisting of the tiny FS is not Dirac dispersion but the electron parabolic dispersion. Our ARPES data demonstrate that $CdSnAs_2$ consists of the spherelike tiny FS at the BZ center.

Next we turn our attention to theoretical calculations of $CdSnAs_2$ and comparisons with ARPES spectra. Since the results of the usual GGA calculation do not reproduce the band gap, we adopt the mBJ exchange-correlation potential [30]. Figure 2(a) shows the band-structure calculation with mBJ + SOC for $CdSnAs_2$ along the ΓX and ΓZ directions. The resultant band dispersion is shifted along the energy scale to be equal to the Fermi wave number obtained from the SdH measurement of our sample [21]. Here, we underline that the shifted band structure explains well the bulk properties of $CdSnAs_2$. The band structures indicate the direct band gap located at the BZ center, and they agree with the previous studies on the DFT calculation with mBJ [17,31]. The electron band across E_F originates from the s-orbital Γ_6 states, and the hole bands are assigned to Γ_7 and Γ_6 states according to the notation of Refs. [17,32,33]. The calculated electron band crosses E_F at the Fermi wave number $k_F = 0.036$ Å^{-1} and the bottom of its band is located at −142 meV. The carrier density and the effective mass are estimated to be $n_{cal} = 3.2 \times 10^{18}$ cm^{-3} ($r_s = 80$) and $m^*_{cal}/m_e = 0.050$, respectively. These show the good correspondence with the previous reports on Hall measurements and SdH oscillations for $CdSnAs_2$ [9–11,14–16]. In addition, the band gap between the electron band (Γ_7) and the hole band (Γ_6) is ∼ 245 meV, which agrees with the previously reported values of 220–260 meV [9,11,13,14]. We compare the ARPES spectrum with the calculated bands in Fig. 2(b). The calculated hole bands of Γ_7 and Γ_6 states around −0.31 eV are shifted down by ∼180 meV for comparison with the ARPES spectra. The observed hole bands are basically consistent with the calculated band dispersions along the ΓX and ΓZ directions. As shown in Fig. 2(c), the ARPES intensity near E_F is identified and the Fermi cutoff was clearly observed in the energy distribution curve (EDC). Moreover, the shoulder structure at ∼ − 110 meV can be seen, corresponding to the bottom of the electron band. However, the calculated electron band does not reproduce the ARPES intensity near E_F. Figure 3(a) shows the ARPES spectrum along the Γ-Z direction, corresponding to the blue arrow in Fig. 1(c). We have fitted the momentum distribution curve (MDC) at E_F by the double Voigt function, which is the Lorentz function convoluted with the instrumental angle resolution. Figure 3(b) shows the fitted result of the MDC at E_F (top panel). The Fermi wave number of $k_F = 0.012$ Å^{-1} is remarkably small. Moreover, we deduced the electron band by the Voigt fitting in the same procedure. The fitted results are depicted as dots and show the parabolic dispersion in Fig. 3(a). Here, the bottom of the electron band is located at $E = -115$ meV. From the band dispersion, we estimated a Fermi velocity $v_F \sim 16.8$ eV Å $= 2.55 \times 10^6$ m/s. The validity of the MDC analysis is provided in Supplemental Material [21]. The Fermi velocity v_F of $CdSnAs_2$ is surprisingly high

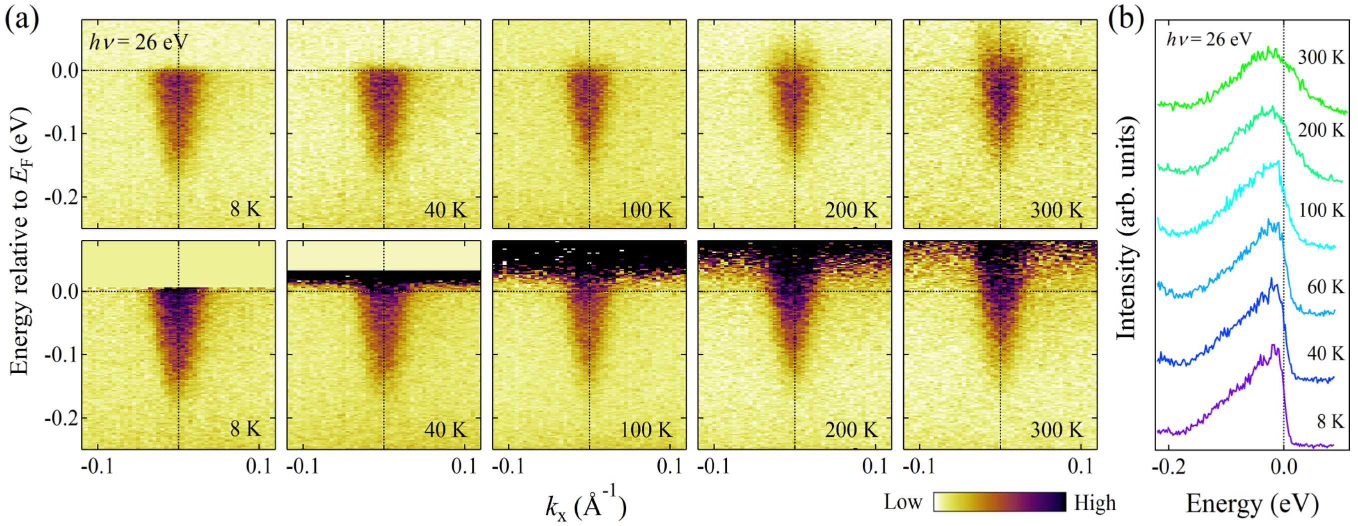

FIG. 4. (a) Temperature dependence of ARPES spectra along Γ-Z direction (top panel). The ARPES spectra divided by FD functions for each temperature convoluted with the energy resolution (bottom panel). (b) Temperature dependence of angle-integrated spectra along Γ-Z direction.

even without a Dirac dispersion and comparable to Dirac materials such as a monolayer graphene [34–37], topological insulators Bi_2Te_3, Bi_2Se_3 [38–40], and Weyl semimetal Cd_3As_2 [41–45]. Further, we calculated an effective mass $m^* = \hbar k_F/v_F$ using the estimated k_F and v_F. This yields an effective mass of $m^*/m_0 \sim 0.005$, which is smaller than that of typical semiconductors by an order of magnitude [21,46,47] and is comparable to graphene [21,37].

Figure 4(a) shows the temperature dependence of the ARPES spectra along the Γ-*Z* direction. To confirm the electronic structure slightly above E_F, we have divided the ARPES spectra by the Fermi-Dirac distribution (FD) function for each temperature with the energy resolution as shown in the lower panel of Fig. 4(a). The divided spectra exhibit spectral intensity above E_F, indicating that the band crosses E_F. In Fig. 4(b), the temperature dependence of angle-integrated spectra shows the thermal broadening derived from the FD function. Since the finite intensity is above E_F in the angle-integrated spectra, the band crossing at E_F is also confirmed.

Here, we focus on the deviation of the ARPES spectrum from the calculated band dispersion. The observed k_F is almost one-third of the band calculation, while the calculated band dispersion is in good agreement with the effective mass and the band gap from the previous transport studies. The smaller FS observed in ARPES suggests the difference from the SdH oscillation measurements and the reduction of the carrier concentration from those. This discrepancy is known to occur in the semiconductors such as InSb, CdTe, and the topological insulator Bi_2Se_3 [48–50]. This is due to the bulk band bending originating from the space-charge accumulation near the surface. The surface depletion layer z_d of ~25 nm is estimated from $z_d^2 = \kappa\epsilon_0\Delta V/en$ as the solution of the Poisson equation. Here, the dc dielectric permittivity κ is 11 [51]. The energy difference ΔV of 115 meV is obtained by shifting the calculated band dispersion to match the observed k_F and the calculated k_F. Moreover, the effective mass of $m^*/m_0 = 0.005$ is remarkably changed from that of $m^*_{cal}/m_0 = 0.050$, which is contrary to the electron-electron interaction on the basis of Landau Fermi liquid theory and the electron-boson interaction. For the 3D electron gas, the r_s dependence of the effective mass m^*/m_0 shows the decrease and then exhibits the increase for the RPA and the *GW* approximations [1,52,53]. On the other hand, the effective mass m^*/m_0 calculated by Yasuhara, Ousaka, and Takada monotonically decreases as a function of r_s ($m^*/m_0 < 1$), which originates from the results of the disappearance of the screening effect and the recovery of the long-range Coulomb interaction [2,4]. Our experimental result suggests that the effective mass decreases ($m^*/m_0 < 1$) in the extremely low-density limit, that is, the effective mass does not diverge ($m^* \to \infty$) in the Wigner crystal region $r_s > 100$. The low-density region $r_s > 5.25$ shows an interesting property of a negative electronic compressibility [54]. The electronic compressibility is defined as $1/\kappa = n^2(\partial\mu/\partial n)$, where μ is the chemical potential. Similar to the shift of 180 meV for the holelike bands in Figs. 2(a) and 2(b), the energy gap between the hole bands and the electron bands changes from 454 meV of ARPES to 245 meV of the band calculation, which can be understood as a decrease of μ. The carrier density n, alternatively, increases in going from the results of ARPES to that of the band calculation. This would be a result of the negative electronic compressibility from ARPES to the bulk band calculation in the low-density region, which was also observed in the other low carrier density materials such as $(Sr_{1-x}La_x)_3Ir_2O_7$ and WSe_2 [55,56].

Finally, we mention the width of the MDC at E_F. Since the width of the MDC at E_F reflects the mean free path $l = 1/\Delta k$, we fitted the MDC at E_F by the two Voigt functions, which is the Lorentz function convoluted with the instrumental angle resolution [Fig. 3(b)]. The width of the Lorentz function Δk and the mean free path l at $T = 8$ K are estimated to be 0.025 Å^{-1} and ~40.7 Å, respectively. On the basis of the Mott-Ioffe-Regel (MIR) criterion [57], the system is metallic for $k_F l > 1$ and reaches the MIR limit for $k_F l \sim 1$. The MIR criterion of $CdSnAs_2$ is $k_F l \sim 0.49$, indicating a strong violation of the MIR limit not due to the short lifetime $\tau = l/\hbar v_F$ but to the small k_F. Thus, $CdSnAs_2$ would be located in the vicinity of the Anderson transition between localized and metallic states.

IV. CONCLUSION

In conclusion, we have studied the electronic structure of ternary chalcopyrite $\mathrm{CdSnAs_2}$ using ARPES combined with the band-structure calculation. The tiny FS consisting of the electron band was observed in the BZ center, which corresponds to the extremely low-density limit in the 3D electron gas. The observed electron bands show the enhanced Fermi velocity v_F and the extremely light electron mass m^*/m_0, which are comparable to the Dirac materials such as graphene, topological insulators, and Weyl semimetals. Our results suggest that the fascinating electronic state with the light electron mass is realized in the extremely low electron density limit at the surface of $\mathrm{CdSnAs_2}$. We believe that the findings will open up new opportunities for the Fermi velocity engineering using the electron gas as well as the electron correlation in the low-density limit of the electron gas such as Wigner crystal.

ACKNOWLEDGMENTS

The authors would like to thank T. Morinari and M. Kobayashi for valuable comments, and D. Shibata, M. Kawamoto, and K. Yamawaki for experimental support. The synchrotron radiation experiments were performed with the approval of HSRC (Proposals No. 16BG025, No. 19BG016, and No. 20AG026) and UVSOR (Proposal No. 29-551). This work was supported by the Kyoto University Research Funds for Young Scientists (Start-up), the Kyoto University Foundation, and the Chubei Itoh Fundation, and Japan Society for the Promotion of Science (JSPS) Grants-in-Aid for Scientific Research (KAKENHI No. JP21K13882, No. 20H01861, and No. 16K05445).

---

[1] L. Hedin, Phys. Rev. **139**, A796 (1965).

[2] H. Yasuhara and Y. Ousaka, Solid State Commun. **64**, 673 (1987).

[3] H. Yasuhara and Y. Ousaka, Int. J. Mod. Phys. B **06**, 3089 (1992).

[4] Y. Takada, Phys. Rev. B **43**, 5979 (1991).

[5] E. Wigner, Phys. Rev. **46**, 1002 (1934).

[6] D. M. Ceperley and B. J. Alder, Phys. Rev. Lett. **45**, 566 (1980).

[7] F. Bloch, Z. Phys. **57**, 545 (1929).

[8] K. Moulopoulos and N. W. Ashcroft, Phys. Rev. Lett. **69**, 2555 (1992).

[9] A. J. Strauss and A. J. Rosenberg, J. Phys. Chem. Solids **17**, 278 (1960).

[10] W. G. Spizer, J. H. Wernick, and R. Wolfe, Solid-State Electron. **2**, 96 (1961).

[11] M. Matyáš and P. Hoschl, Czech. J. Phys. **12**, 788 (1962).

[12] Y. I. Polygalov and A. S. Poplavnoi, Sov. Phys. J. **24**, 1139 (1981).

[13] W. D. C. B. Gunatilleke, D. Hobbis, H. Poddig, A. Tinkess, M. Beekman, H. Wang, K. Wei, R. E. Baumbach, and G. S. Nolas, Inorg. Chem. **59**, 3079 (2020).

[14] P. L. Hugon, J. Phys. Chem. Solids **27**, 1205 (1966).

[15] F. A. P. Blom, H. Nachtegaele, and J. T. Devreese, Phys. Rev. B **32**, 2334 (1985).

[16] Y. Nakashima and C. Hamaguchi, J. Phy. Soc. Jpn. **56**, 3248 (1987).

[17] W. Feng, D. Xiao, J. Ding, and Y. Yao, Phys. Rev. Lett. **106**, 016402 (2011).

[18] N. S. Ziani, H. Bouhani-Benziane, M. Baira, A. E. K. Belfedal, M. Sahnoun, Electronic and Thermoelectric Properties of $\mathrm{CdSnAs_2}$, in *Proceedings of the Third International Symposium on Materials and Sustainable Development. SMSD 2017*, edited by B. Abdelbaki, B. Safi, and M. Saidi (Springer, Cham, 2018), pp. 365–371.

[19] Z. Yao, X. Zhang, J. Shen, B. Chen, R. Ang, and W. Li, J. Alloys Compd. **809**, 151772 (2019).

[20] K. Homma and F. Izumi, J. Appl. Crystallogr. **44**, 1272 (2011).

[21] See Supplemental Material at http://link.aps.org/supplemental/10.1103/PhysRevMaterials.8.044604 for the photon energy dependence of ARPES, the SdH oscillation for $\mathrm{CdSnAs_2}$, the Fermi velocity, the effective mass for the typical semiconductor, graphene, and Dirac materials, and the simulation of ARPES spectra, which includes Refs. [22–24].

[22] V. N. Strocov, J. Electron Spectrosc. Relat. Phenom. **130**, 65 (2003).

[23] H. Wadati, T. Yoshida, A. Chikamatsu, H. Kumigashira, M. Oshima, H. Eisaki, Z.-X. Shen, T. Mizokawa, and A. Fujimori, Phase Trans. **79**, 617 (2006).

[24] T. Mitsuhashi, M. Minohara, R. Yukawa, M. Kitamura, K. Horiba, M. Kobayashi, and H. Kumigashira, Phys. Rev. B **94**, 125148 (2016).

[25] P. Blaha, K. Schwarz, G. K. H. Madsen, D. Kvasnicka, and J. Luitz, WIEN2k (Technische Universität Wien, Austria, 2002).

[26] J. P. Perdew, K. Burke, and M. Ernzerhof, Phys. Rev. Lett. **77**, 3865 (1996).

[27] A. D. Becke and E. R. Johnson, J. Chem. Phys. **124**, 221101 (2006).

[28] F. Tran and P. Blaha, Phys. Rev. Lett. **102**, 226401 (2009).

[29] A. Continenza, S. Massidda, A. J. Freeman, T. M. de Pascale, F. Meloni, and M. Serra, Phys. Rev. B **46**, 10070 (1992).

[30] V. L. Shaposhnikov, A. V. Krivosheeva, V. E. Borisenko, J.-L. Lazzari, and F. A. d'Avitaya, Phys. Rev. B **85**, 205201 (2012).

[31] W. Feng, J. Wen, J. Zhou, D. Xiao, and Y. Yao, Comput. Phys. Commun. **183**, 1849 (2012).

[32] H. Kildal, Phys. Rev. B **10**, 5082 (1974).

[33] S. Limpijumnong and W. R. L. Lambrecht, Phys. Rev. B **65**, 165204 (2002).

[34] K. R. Knox, S. Wang, A. Morgante, D. Cvetko, A. Locatelli, T. O. Mentes, M. A. Niño, P. Kim, and R. M. Osgood, Jr., Phys. Rev. B **78**, 201408(R) (2008).

[35] M. Sprinkle, D. Siegel, Y. Hu, J. Hicks, A. Tejeda, A. Taleb-Ibrahimi, P. Le Fèvre, F. Bertran, S. Vizzini, H. Enriquez,

S. Chiang, P. Soukiassian, C. Berger, W. A. de Heer, A. Lanzara, and E. H. Conrad, Phys. Rev. Lett. **103**, 226803 (2009).

[36] C. Hwang, D. A. Siegel, S. Mo, W. Regan, A. Ismach, Y. Zhang, A. Zettl, and A. Lanzara, Sci. Rep. **2**, 590 (2012).

[37] D. C. Elias, R. V. Gorbachev, S. V. Mayorov, A. S. Morozov, A. A. Zhukov, P. Blake, L. A. Ponomarenko, I. V. Grigorieva, K. S. Novoselov, F. Guinea, and A. K. Geim, Nat. Phys. **7**, 701 (2011).

[38] D.-X. Qu, Y. S. Hor, Jun Xiong, R. J. Cava, and N. P. Ong, Science **329**, 821 (2010).

[39] K. Kuroda, M. Arita, K. Miyamoto, M. Ye, J. Jiang, A. Kimura, E. E. Krasovskii, E. V. Chulkov, H. Iwasawa, T. Okuda, K. Shimada, Y. Ueda, H. Namatame, and M. Taniguchi, Phys. Rev. Lett. **105**, 076802 (2010).

[40] B. J. Lawson, Y. S. Hor, and L. Li, Phys. Rev. Lett. **109**, 226406 (2012).

[41] S. Borisenko, Q. Gibson, D. Evtushinsky, V. Zabolotnyy, B. Büchner, and R. J. Cava, Phys. Rev. Lett. **113**, 027603 (2014).

[42] M. Neupane, S. Xu, R. Sankar, N. Alidoust, G. Bian, C. Liu, I. Belopolski, T. Chang, H. Jeng, H. Lin, A. Bansil, F. Chou, and M. Z. Hasan, Nat. Commun. **5**, 3786 (2014).

[43] Z. K. Liu, J. Jiang, B. Zhou, Z. J. Wang, Y. Zhang, H. M. Weng, D. Prabhakaran, S-K. Mo, H. Peng, P. Dudin, T. Kim, M. Hoesch, Z. Fang, X. Dai, Z. X. Shen, D. L. Feng, Z. Hussain, and Y. L. Chen, Nat. Mater **13**, 677 (2014).

[44] L. P. He, X. C. Hong, J. K. Dong, J. Pan, Z. Zhang, J. Zhang, and S. Y. Li, Phys. Rev. Lett. **113**, 246402 (2014).

[45] S. Roth, H. Lee, A. Sterzi, M. Zacchigna, A. Politano, R. Sankar, F. C. Chou, G. Di Santo, L. Petaccia, O. V. Yazyev, and A. Crepaldi, Phys. Rev. B **97**, 165439 (2018).

[46] I. Vurgaftman, J. R. Meyer, and L. R. Ram-Mohan, J. Appl. Phys. **89**, 5815 (2001).

[47] Y.-S. Kim, M. Marsman, G. Kresse, F. Tran, and P. Blaha, Phys. Rev. B **82**, 205212 (2010).

[48] P. D. C. King, T. D. Veal, M. J. Lowe, and C. F. McConville, J. Appl. Phys. **104**, 083709 (2008).

[49] R. K. Swank, Phys. Rev. **153**, 844 (1967).

[50] J. G. Analytis, J.-H. Chu, Y. Chen, F. Corredor, R. D. McDonald, Z. X. Shen, and I. R. Fisher, Phys. Rev. B **81**, 205407 (2010).

[51] A. S. Verma and S. R. Bhardwaj, Phys. Status Solidi B **243**, 4025 (2006).

[52] M. Gell-Mann and K. A. Brueckner, Phys. Rev. **106**, 364 (1957).

[53] T. Endo, M. Horiuchi, Y. Takada, and H. Yasuhara, Phys. Rev. B **59**, 7367 (1999).

[54] Y. Takada, Phys. Rev. B **43**, 5962 (1991).

[55] J. He, T. Hogan, T. R. Mion, H. Hafiz, Y. He, J. D. Denlinger, S.-K. Mo, C. Dhital, X. Chen, Q. Lin, Y. Zhang, M. Hashimoto, H. Pan, D. H. Lu, M. Arita, K. Shimada, R. S. Markiewicz, Z. Wang, K. Kempa, M. J. Naughton *et al.*, Nat. Mater. **14**, 577 (2015).

[56] J. M. Riley, W. Meevasana, L. Bawden, M. Asakawa, T. Takayama, T. Eknapakul, T. K. Kim, M. Hoesch, S.-K. Mo, H. Takagi, T. Sasagawa, M. S. Bahramy, and P. D. C. King, Nat. Nanotechnol. **10**, 1043 (2015).

[57] A. F. Ioffe and A. R. Regel, Prog. Semicond. **4**, 237 (1960).